

## Research paper

## Permeability and porosity of hydrate-bearing sediments in the northern Gulf of Mexico

Hugh Daigle <sup>a,\*</sup>, Ann Cook <sup>b</sup>, Alberto Malinverno <sup>c</sup><sup>a</sup> Department of Petroleum and Geosystems Engineering, University of Texas at Austin, 200 E Dean Keeton Street, Stop C0300, Austin, TX 78712-1585, USA<sup>b</sup> School of Earth Sciences, The Ohio State University, 275 Mendenhall Laboratory, 125 South Oval Mall, Columbus, OH 43210, USA<sup>c</sup> Lamont-Doherty Earth Observatory of Columbia University, PO Box 1000, 61 Route 9W, Palisades, NY 10964-1000, USA

## ARTICLE INFO

## Article history:

Received 7 August 2015

Received in revised form

2 October 2015

Accepted 6 October 2015

Available online 14 October 2015

## Keywords:

Walker Ridge

Methane hydrates

Permeability

Effective medium theory

Integrated Ocean Drilling Program

## ABSTRACT

Hydrate-bearing sands are being actively explored because they contain the highest concentrations of hydrate and are the most economically recoverable hydrate resource. However, relatively little is known about the mechanisms or timescales of hydrate formation, which are related to methane supply, fluid flux, and host sediment properties such as permeability. We used logging-while-drilling data from locations in the northern Gulf of Mexico to develop an effective medium theory-based model for predicting permeability based on clay-sized sediment fraction. The model considers permeability varying between sand and clay endpoint permeabilities that are defined from laboratory data. We verified the model using permeability measurements on core samples from three boreholes, and then used the model to predict permeability in two wells drilled in Walker Ridge Block 313 during the Gulf of Mexico Gas Hydrate Joint Industry Project Leg II expedition in 2009. We found that the cleanest sands (clay-sized fraction <0.05) had intrinsic (hydrate-free) permeability contrasts of 5–6 orders of magnitude with the surrounding clays, which is sufficient to provide focused hydrate formation due to advection of methane from a deep source or diffusion of microbial methane from nearby clay layers. In sands where the clay-sized fraction exceeds 0.05, the permeability reduces significantly and focused flow is less pronounced. In these cases, diffusion of dissolved microbial methane is most likely the preferred mode of methane supply for hydrate formation. Our results provide important constraints on methane supply mechanisms in the Walker Ridge area and have global implications for evaluating rates of methane migration and hydrate formation in hydrate-bearing sands.

© 2015 Elsevier Ltd. All rights reserved.

## 1. Introduction

Permeability is an intrinsic rock property that controls rates of fluid flow and excess pore pressure dissipation. Constraining permeability is important in many subsurface applications, including groundwater management, oil and gas exploration, and geohazard mitigation. Permeability may be determined directly in the laboratory or by downhole tools, or indirectly through correlation with other properties such as porosity and grain size (Dullien, 1992). Most permeability estimates tend to be indirect since downhole testing is time-consuming and expensive, and laboratory tests require good quality physical samples and can require several days per test. Therefore, high quality indirect permeability

determinations are essential to reducing uncertainty in fluid flow and pore pressure calculations. Unfortunately, many indirect methods of permeability determination involve empirical terms that require ad hoc calibration with some measurements, which often means that the results are reliable only in the specific location in which the calibration data were collected. Good permeability prediction therefore still requires a large number of direct measurements.

In methane hydrate-bearing sediments, permeability determines the rate at which methane may be supplied to the methane hydrate stability zone (MHSZ) and can influence the localization of hydrate in discrete layers with high hydrate saturation (>50% of pore volume; Cook and Malinverno, 2013; Chatterjee et al., 2014). Permeability is especially important in systems where methane is supplied to the MHSZ advectively from deeper and/or distant sources. Permeability controls the methane flux, which in turn determines the rate of hydrate formation, the

\* Corresponding author.

E-mail address: [daigle@austin.utexas.edu](mailto:daigle@austin.utexas.edu) (H. Daigle).

amount of hydrate that forms, and its local distribution (Xu and Ruppel, 1999; Nimblett and Ruppel, 2003; Daigle and Dugan, 2010). In addition, the permeability of hydrate-bearing sediments and associated hydrate-free bounding layers is important for predicting the response of these systems to various perturbations including gas production, temperature changes due to changes in ocean temperature, and pressure changes due to changes in relative sea level (e.g., Moridis et al., 2004; Xu and Germanovich, 2006; Reagan and Moridis, 2008; Liu and Flemings, 2009). In particular, simulations suggest the permeability of clays surrounding hydrate-bearing sands strongly influences the decline of gas production rates over time as a result of variations in water influx (Myshakin et al., 2012). In the northern Gulf of Mexico, shallow sand units form important conduits for focused fluid flow and reservoirs that can host high concentrations of methane hydrate (Behrmann et al., 2006; Frye, 2008; Boswell et al., 2012a). Accurate characterization of the permeability structure of the sands and the surrounding fine-grained sediments helps determine the rate at which hydrate deposits will form (Chatterjee et al., 2014) and the rate of pore pressure buildup, dissipation, and fluid flow in response to external forcing. Moreover, understanding the permeability throughout the MHSZ elucidates the rates and timescales associated with methane migration and hydrate formation in the northern Gulf of Mexico and allows us to predict how these systems will respond to changes in hydrate stability conditions. The method we describe here estimates permeability at fully water-saturated conditions; the permeability reduction due to methane hydrate formation in the pore space is described in the discussion, but a full treatment is beyond our scope.

Permeability in marine sediments can be predicted using effective medium theory by considering the sediment as a binary mixture of clay-sized and larger particles (Daigle and Scream, 2015b). Using endpoint permeabilities constrained by laboratory measurements, we show that this method may be used to predict permeability accurately in shallow sediments in the northern Gulf of Mexico. We apply our analysis to three boreholes from the Mississippi Canyon and Keathley Canyon areas with measured permeabilities and show that the method yields satisfactory results. We then use the model to predict permeability in two logging-while-drilling (LWD) boreholes at Walker Ridge Block 313 that were drilled in 2009 during the United States Department of Energy (DOE)/Chevron-led Gulf of Mexico Gas Hydrate Joint Industry Project (JIP) Leg II. We show that the sand layers encountered in the Walker Ridge wells have permeabilities on the order of  $10^{-13}$  to  $10^{-12}$  m<sup>2</sup> (~100–1000 mD; 1 mD =  $9.869 \times 10^{-16}$  m<sup>2</sup>), in contrast with the surrounding clays, which have permeabilities of  $\sim 10^{-18}$  m<sup>2</sup> (~0.001 mD). Our inferred permeability contrasts between sands and clays (up to 6 orders of magnitude) are similar to intrinsic permeability contrasts between sands and clays determined for the hydrate reservoirs in the eastern Nankai Trough (Konno et al., 2015b). These results provide valuable constraints for modeling gas production from hydrate reservoirs in the northern Gulf of Mexico, particularly on the permeability of the clays surrounding the hydrate-bearing sands, which previous modeling efforts have assigned permeabilities ranging from 0 to  $10^{-14}$  m<sup>2</sup> (0–10 mD) and have been previously unconstrained (e.g., Moridis et al., 2010; Gaddipati et al., 2011; Myshakin et al., 2012). Overall this work has important implications for focused flow and hydrate distribution in sediments in the northern Gulf of Mexico.

## 2. Theory

Effective medium theory (EMT) allows determination of the bulk properties of a multicomponent, disordered medium from the properties of the individual components as well as their relative

concentrations and degree of interconnectedness. In Kirkpatrick's EMT formulation (Kirkpatrick, 1971, 1973), the permeability  $k_e$  of a multi-component medium satisfies the relation

$$\sum_i f_i \frac{k_i - k_e}{k_i + (Z/2 - 1)k_e} = 0, \quad (1)$$

where  $k_i$  and  $f_i$  are the permeability and volume fraction of the  $i$ th component, respectively, and  $Z$  is the average pore coordination number (average number of neighboring pores to which a given pore is connected). Note that although Kirkpatrick's original work dealt with electrical conductivity rather than permeability (e.g., Kirkpatrick, 1971), Eq. (1) has successfully been applied to permeability prediction in porous media (e.g., David et al., 1990; Renard and de Marsily, 1997; Daigle and Scream, 2015b).

Daigle and Scream (2015b) showed that the permeability of shallow marine sediments could be predicted with a two-component EMT that considers the sediments as mixtures of clay-sized particles and (silt + sand)-sized particles. In their formulation, Eq. (1) takes the form

$$(1 - f_c) \frac{k_s - k_e}{k_s + [f_c/(1 - f_c)]k_e} + f_c \frac{k_c - k_e}{k_c + [f_c/(1 - f_c)]k_e} = 0, \quad (2)$$

where  $f_c$  is the mass fraction of clay-sized particles (equivalent diameter <4  $\mu$ m), and  $k_s$  and  $k_c$  are the endmember permeabilities of the (silt + sand)-sized fraction and clay-sized fraction, respectively. The transformation from a volume-based equation (Eq. (1)) to a mass-based equation (Eq. (2)) is based on the assumptions that the clay-sized and (silt + sand)-sized fractions have roughly the same solid grain density, and that the endmember clay-sized and (silt + sand)-sized components have the same porosity. These assumptions are reasonable for shallow sediments in the northern Gulf of Mexico. John and Adatte (2009) determined mineralogy from X-ray diffraction in fine-grained sediments from Mississippi Canyon and showed that the clay-sized fraction is dominantly phyllosilicate minerals, and the (silt + sand)-sized fraction is roughly 47% quartz, 8% potassic feldspar, 11% plagioclase, 16% calcite, and 19% dolomite. This yields a solid grain density of 2.70 g cm<sup>-3</sup> for the clay-sized fraction (assuming mainly mixed-layer illite-smectite) and 2.72 g cm<sup>-3</sup> for the (silt + sand)-sized fraction. Similarly, Schneider et al. (2011) and Reece et al. (2013) showed that grain-scale porosity variations that occur in mudstones due to stress shielding of clay grains around silt grains are extremely localized and that the overall permeability behavior can be modeled by assuming that the endmembers have equal porosities. The pore coordination number is assumed to obey the relationship  $Z = 2/(1 - f_c)$ , which implies that connected flow pathways exist through both the clay-sized and (silt + sand)-sized components without preferential flow through either component (e.g., McLachlan, 1988). Eq. (2) has an analytical solution in the form of a quadratic equation in  $k_e$ .

## 3. Data sources

We used data from six locations in the northern Gulf of Mexico: Integrated Ocean Drilling Program (IODP) Expedition 308 Sites U1322 and U1324, JIP Leg 1 Site Keathley Canyon Block 151 Holes 2 and 3 (KC151-2 and KC151-3), and JIP Leg 2 Site Walker Ridge Block 313 Holes G and H (WR313-G and WR313-H) (Fig. 1). All six locations were situated in salt-withdrawal minibasins (Expedition 308 Scientists, 2006b; Hutchinson et al., 2008; Boswell et al., 2012a) and have been influenced by similar sedimentation processes; the largest difference among the locations is sedimentation rate due to their relative proximity to the present-day Mississippi River delta.

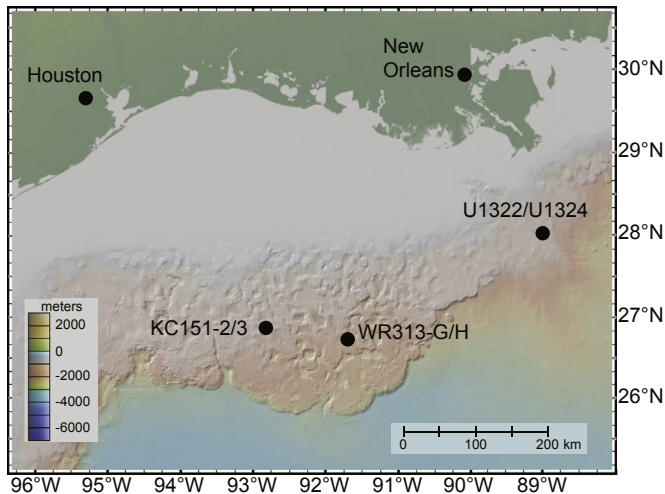


Fig. 1. Location of the boreholes considered.

Sites U1322 and U1324 were drilled in 2005 as part of IODP Expedition 308 to investigate the physical properties of sediments in an area with an extensive history of submarine mass movements (Behrmann et al., 2006; Expedition 308 Scientists, 2006b, 2006c). They were located in Mississippi Canyon Blocks 897 and 899 in water depths of 1319 m (U1322) and 1055 m (U1324). Logging-while-drilling (LWD) logs were collected at both locations (Expedition 308 Scientists, 2006a). LWD logs were obtained to depths of 238 m below sea floor (mbsf) at Site U1322 (Fig. 2) and 612 mbsf at Site U1324 (Fig. 3). Site U1322 penetrated mainly muds associated with Holocene hemipelagic sediments and distal levees with some mass transport deposits (Expedition 308 Scientists, 2006b). Site U1324 penetrated similar sediments with the addition of interbedded silts and sands below 365 mbsf that are interpreted as overbank deposits associated with older, low-relief channels (Expedition 308 Scientists, 2006c). Continuous core was collected at both sites. Grain size measurements were performed by Sawyer et al. (2008) using the hydrometer method (ASTM International, 2003). Permeability data were obtained by Long et al. (2008b) from uniaxial, constant rate-of-strain consolidation tests (ASTM International, 2006).

KC151-2 and KC151-3 were drilled in 2005 as part of JIP Leg 1 (Claypool, 2006; Ruppel et al., 2008). The wells were located in water depths of 1321.8 m (KC151-2) and 1322.5 m (KC151-3). LWD logs were collected in KC151-2 to a depth of 459.8 mbsf (Claypool, 2006) (Fig. 4). Several sand layers were encountered between 95 and 150 mbsf in the wells; the methane hydrate saturation in these sands is inconclusive due to poor borehole quality (Lee and Collett, 2008). A deeper interval 220–300 mbsf contains steeply dipping hydrate-filled fractures with some associated thin, hydrate-bearing sands (Cook et al., 2008). The base of the MHSZ is at 392 mbsf, based on LWD-seismic integration and the position of the bottom-simulating reflection (Lee and Collett, 2008). Continuous core was collected in KC151-3 to a depth of 441.4 mbsf. Grain size measurements were performed by Winters et al. (2008) using a Coulter counter. Permeability data were obtained by Dugan (2008) and Daigle and Dugan (2009) from uniaxial, constant rate-of-strain consolidation tests (ASTM International, 2006).

WR313-G and WR313-H were drilled in 2009 as part of JIP Leg 2 (Boswell et al., 2012a). The wells were located in water depths of 2000 m (WR313-G) and 1966 m (WR313-H). WR313-H is located updip of WR313-G, with seismic data indicating thinning of sedimentary layers in the updip direction as a consequence of synsedimentary salt deformation (Boswell et al., 2012b). LWD logs were collected in both wells, to depths of 1093 mbsf (WR313-G) and 996.4 mbsf (WR313-H). Gamma ray, bulk density, density caliper, and ultrasonic caliper were measured in both wells (Collett et al., 2012) (Fig. 5). Several sand layers were encountered in each well, with sands in WR313-H being structurally higher and generally thinner than correlative units in WR313-G. The Blue unit, at a depth of 805 mbsf in WR313-G and 680 mbsf in WR313-H, was interpreted as proximal to distal turbidite channel levees with some sheet sands (Boswell et al., 2012b). On the basis of resistivity and acoustic log analysis, sands of the Blue unit were interpreted to have methane hydrate saturations 20–80% in both WR313-G and WR313-H, though the overall unit is considerably thinner in WR313-H (Collett et al., 2012). The Orange unit, at a depth of 945 mbsf in WR313-G and 785 mbsf in WR313-H, was interpreted as proximal turbidite channel levees at WR313-H; the Orange unit occurred as a mud-filled channel at WR313-G (Boswell et al., 2012b). The sand in the Orange unit at WR313-H is cleaner than in the Blue unit. Methane hydrate saturation based on resistivity and acoustic log analysis was interpreted to be >80% in the upper lobe of the sand and 25–80% in the lower lobe of the sand (Cook

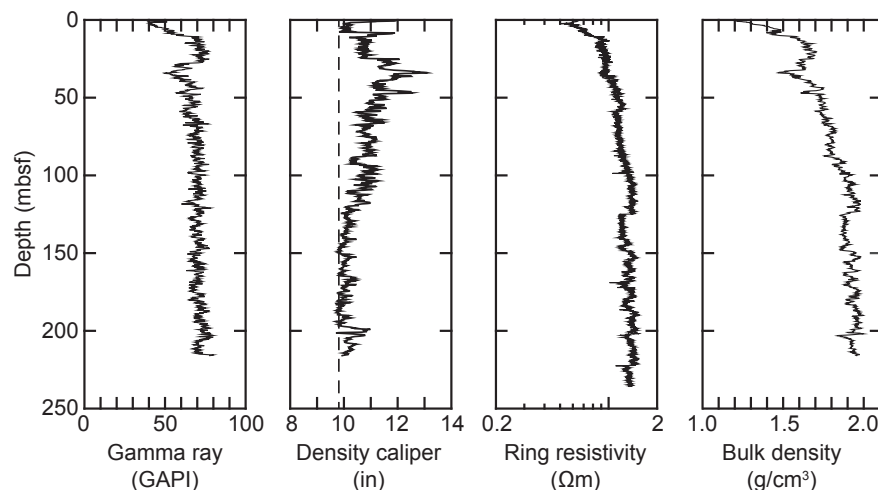
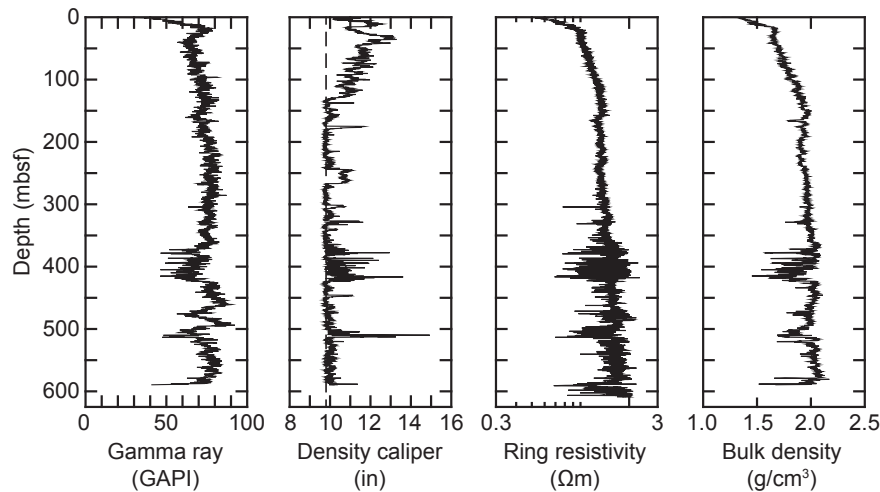
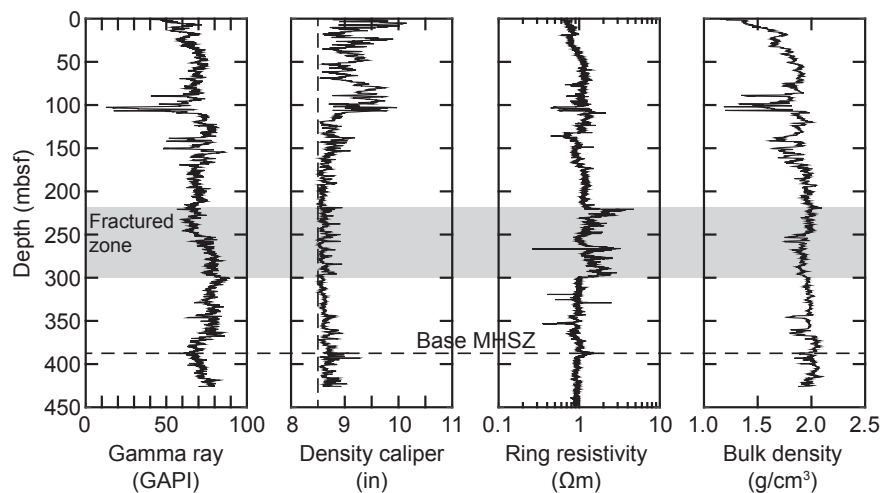


Fig. 2. LWD logs for U1322. Left to right: gamma ray, density caliper, ring resistivity (from resistivity-at-bit), bulk density. Dashed line in density caliper log indicates bit size (9.875").



**Fig. 3.** LWD logs for U1324. Left to right: gamma ray, density caliper, ring resistivity (from resistivity-at-bit), bulk density. Dashed line in density caliper log indicates bit size (9.875").



**Fig. 4.** LWD logs for KC151-2. Left to right: gamma ray, density caliper, ring resistivity (from resistivity-at-bit), bulk density. Dashed line in density caliper log indicates bit size (8.5"). The interval with fracture-hosted hydrates (Cook et al., 2008) is shaded gray.

et al., 2012). The Green unit was encountered only in WR313-H at a depth of 950 mbsf, about 75 m below the interpreted base of the MHSZ. It was interpreted as proximal turbidite channel levees (Boswell et al., 2012b), and was determined to be completely water-saturated based on resistivity log analysis (Collett et al., 2012). A shallower, mud-rich interval containing subvertical hydrate-filled fractures was encountered in both wells, at depths of 257–376 mbsf (WR313-G) and 168–314 mbsf (WR313-H) (Figs. 5 and 6). The base of the MHSZ was estimated at 900 mbsf in WR313-G and 876 mbsf in WR313-H based on extrapolation of the bottom-simulating reflection observed in seismic data (Collett et al., 2012). No cores were collected in either WR313-G or WR313-H.

#### 4. Data processing

The use of Eq. (2) to predict permeability requires knowledge of porosity and clay-sized fraction, as well as suitable endpoint permeabilities for the clay-sized and (silt + sand)-sized fractions. We determined porosity from bulk density logs, and clay-sized fraction from gamma ray logs. The porosity values required correction for

the presence of hydrate in some wells as well as zones where the log quality was poor. The gamma ray values required normalization and comparison with grain-size measurements to determine clay-sized fraction.

##### 4.1. Porosity determination

We determined porosity  $\phi$  [ $\text{cm}^3 \text{cm}^{-3}$ ] from bulk density log values  $\rho_b$  [ $\text{g cm}^{-3}$ ] as

$$\phi = \frac{\rho_g - \rho_b}{\rho_g - \rho_f}, \quad (3)$$

where  $\rho_g$  is the solid grain density [ $\text{g cm}^{-3}$ ] and  $\rho_f$  is the pore fluid density [ $\text{g cm}^{-3}$ ]. We assumed  $\rho_g = 2.65 \text{ g cm}^{-3}$  in sands,  $2.70 \text{ g cm}^{-3}$  in clays, and  $\rho_f = 1.03 \text{ g cm}^{-3}$ . The resulting porosity values had to be corrected for 1) the presence of high saturation hydrate and 2) poor hole conditions, particularly in water-saturated sands. Hydrate affects the measured bulk density because it has a lower density than seawater ( $0.925 \text{ g cm}^{-3}$  at 5 MPa and 273 K; Helgerud et al., 2009), so the density of hydrate bearing sediment



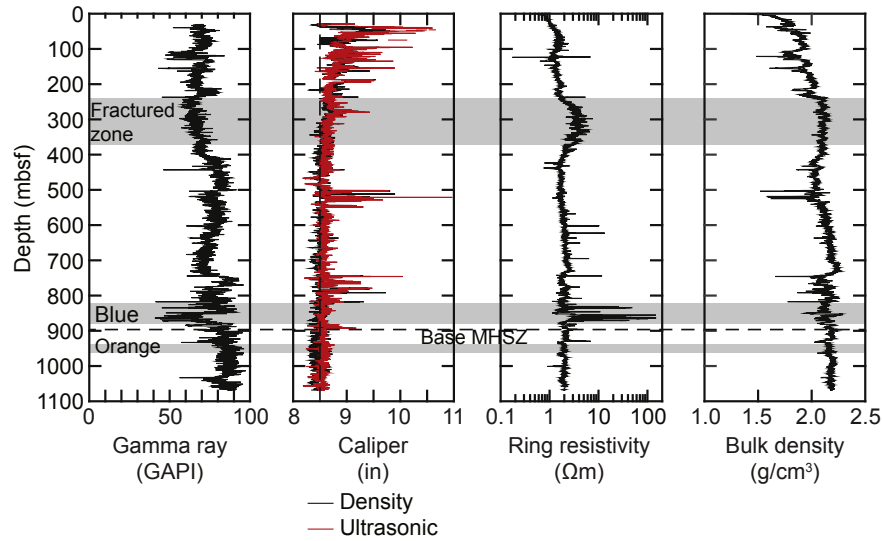


**Fig. 5.** LWD logs for WR313-G. Left to right: gamma ray, density and ultrasonic calipers, ring resistivity (from resistivity-at-bit), bulk density. Dashed line in caliper log indicates bit size (8.5"). Significant lithological units are highlighted in gray.

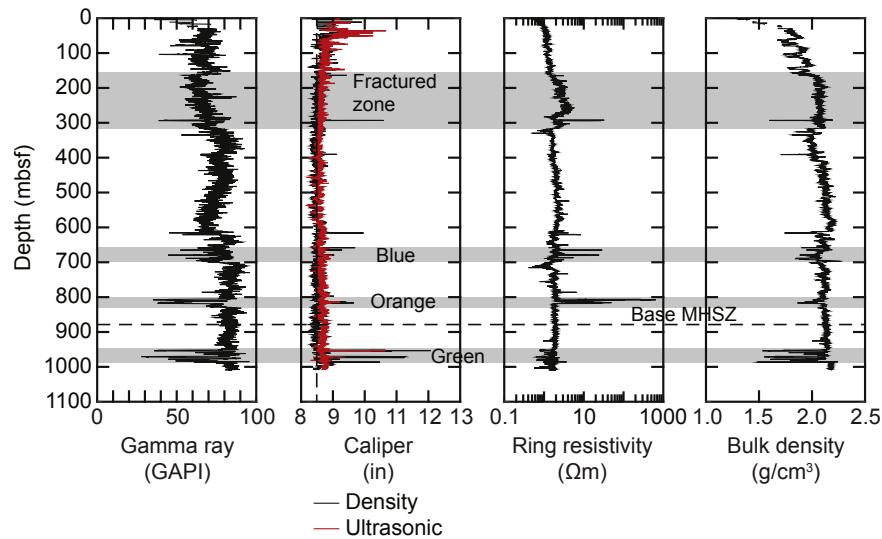


**Fig. 6.** LWD logs for WR313-H. Left to right: gamma ray, density and ultrasonic calipers, ring resistivity (from resistivity-at-bit), bulk density. Dashed line in caliper log indicates bit size (8.5"). Significant lithological units are highlighted in gray.

will be lower than that of the same sediment when completely water-saturated. To correct the porosity for the presence of hydrate, we expressed the bulk density of the sediment as the volumetrically-weighted sum of the densities of the sediment components (solid grains, water, and hydrate):

$$\rho_b = (1 - \phi)\rho_g + \phi(S_w\rho_f + (1 - S_w)\rho_h), \quad (4)$$

where  $\rho_h$  is the density of hydrate [ $\text{g cm}^{-3}$ ] and  $S_w$  is the water saturation (fraction of pore volume occupied by water) [ $\text{cm}^3 \text{cm}^{-3}$ ]. We combined Eq. (4) with Archie's equation and solved iteratively for porosity:

$$\rho_b = (1 - \phi)\rho_g + \phi\left(\left[\frac{aR_w}{\phi^m R_T}\right]^{1/n} \rho_f + \left(1 - \left[\frac{aR_w}{\phi^m R_T}\right]^{1/n}\right) \rho_h\right), \quad (5)$$

where  $R_w$  is the pore fluid resistivity [ $\Omega \cdot \text{m}$ ],  $R_T$  is the measured

formation resistivity [ $\Omega \cdot \text{m}$ ], and  $a$ ,  $m$ , and  $n$  are the Archie parameters. For  $R_T$  we used the ring resistivity curve. Archie parameters were assumed to be  $a = 1$ ,  $m = 2$ , and  $n = 2$  (e.g., Edwards, 1997) since we restricted our corrections to the sands with high hydrate saturation and no specific Archie parameters are known for these sands. Pore fluid resistivity was determined using the method of Fofonoff and Millard (1983) assuming salinity of 35 parts per thousand. In situ temperature was determined assuming a seafloor temperature of 4 °C and a geothermal gradient of 17.9 °C  $\text{km}^{-1}$ . Comparison between the corrected porosity and the original porosity for the Blue sand in WR313-G and the Orange sand in WR313-H, where the corrections were most pronounced, are shown in Fig. 7. The correction generally resulted in a decrease in porosity of less than 0.03.

Shallow, water-saturated sands are typically uncemented and lack the cohesion of clays causing the sand to wash out during drilling. As a result, the borehole is often enlarged in water-saturated sands, which results in an anomalously low bulk

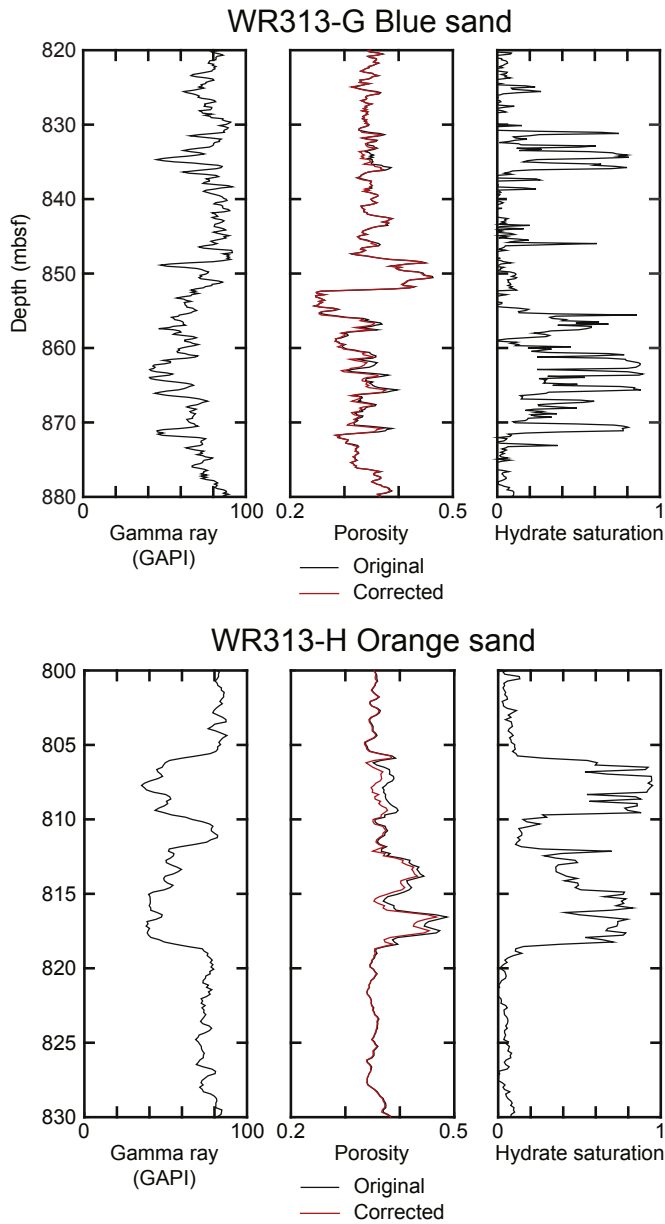


**Fig. 7.** Example of porosity corrections for hydrate saturation in the Blue sands at WR313-G (top) and the Orange sands at WR313-H (bottom). Left to right: gamma ray, porosity (original density porosity and corrected value), and hydrate saturation. (For interpretation of the references to colour in this figure legend, the reader is referred to the web version of this article.)

density reading and a correspondingly anomalously high porosity (e.g., Lee and Collett, 2008). To correct the porosity values in sand layers with enlarged borehole, we used a porosity-effective stress relationship determined from laboratory measurements made by Zimmer (2003) on Holocene sand from the Gulf of Mexico. This sand had a median grain diameter of 82  $\mu\text{m}$ , which is within the range of grain sizes typical of shallow sands in the northern Gulf of Mexico (Stow et al., 1986; Sawyer et al., 2008). We found the following relationship between porosity and vertical effective stress  $\sigma_v'$  [Pa]:

$$\phi = 0.4305 - 0.0001156\sigma_v'^{0.3776}, \quad (6)$$

with a coefficient of determination ( $R^2$ ) of 0.989 (Fig. 8a). We

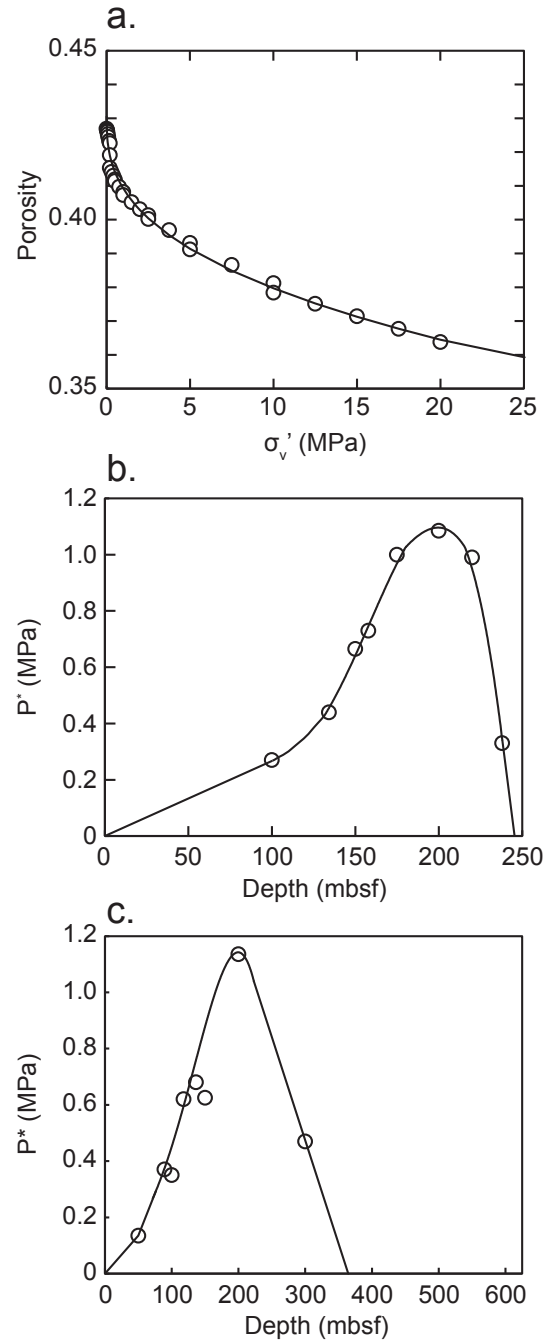


**Fig. 8.** (a) Porosity-effective stress model for sands determined from laboratory data of Zimmer (2003). This relationship was used to determine corrected porosities in water-saturated sands with poor borehole conditions. (b) Overpressure versus depth at U1322. Circles are in situ measurements from Long et al. (2008a); solid line is model used for our calculations. (c) Overpressure versus depth at U1324. Circles are in situ measurements from Long et al. (2008a); solid line is model used for our calculations.

determined  $\sigma_v'$  as a function of depth  $z$  below seafloor [m] as

$$\sigma_v'(z) = \int_0^z \rho_b(z')g dz' - \rho_f g z - P^*(z), \quad (7)$$

where  $g$  is the acceleration due to gravity [ $\text{m s}^{-2}$ ],  $P^*$  is the overpressure (fluid pressure in excess of hydrostatic) [Pa], and  $z'$  is the variable being integrated from 0 to  $z$ . Shallow overpressure is

common in the northern Gulf of Mexico (e.g., Ostermeier et al., 2002; Orange et al., 2003), so it was necessary to determine the degree of overpressure at each of our locations. Detailed pore pressure measurements were available at Sites U1322 and U1324 (Long et al., 2008a). Based on these measurements we fit a model to determine  $P^*$  continuously with depth at these locations (Fig. 8b,c). No detailed measurements of  $P^*$  were available for the Keathley Canyon or Walker Ridge locations. Dugan (2008) estimated the overpressure gradient at KC151 as  $4300 \text{ Pa m}^{-1}$  based on observations of flow out of a borehole filled with weighted drilling fluid. At WR313 we assumed hydrostatic pore pressure because no other information was available. The resulting values of  $\sigma_v'$  were all less than 10 MPa, which fell within the range of effective stresses tested by Zimmer (2003) and allowed the use of Eq. (6) for sand porosity calculation without extrapolation.

After computing  $\sigma_v'$  and the sand porosity trend at each location, we replaced the porosities measured in water-saturated sands with poor borehole conditions with the computed sand porosity when the gamma ray was lower than 55 GAPI and the caliper measured at least 0.25" greater than the bit size. Since both density and ultrasonic calipers were measured at WR313-G and WR313-H, the measured porosity was replaced if either caliper read above this limit in sands. The porosity correction was applied mainly in the sands below 350 mbsf in U1324, shallow sands around 100 mbsf in KC151-2, and in the Green sand in WR313-H (Fig. 9).

#### 4.2. Gamma ray normalization

Since the gamma ray logs were measured at different times by different tools at the locations we studied, we normalized the log values to allow for consistent calculation of clay-sized fraction. Histograms of the raw gamma ray logs (Fig. 10a) show the effects of measuring gamma ray logs with different tools – Sites U1322, U1324, and KC151-2 all have gamma ray from one type of tool, while WR313-G and WR313-H have gamma ray from a different type of tool. To eliminate this discrepancy, we stretched the lower curves (U1322, U1324, and KC151-2) to match the maximum value of the higher curves (WR313-G, WR313-H). This resulted in the final, normalized gamma ray distribution (Fig. 10b) that we used for our clay-sized fraction determination.

#### 4.3. Clay-sized fraction determination

To derive a relationship between normalized gamma ray and

clay-sized fraction, we used grain size measurements from U1322, U1324, and KC151-3 (Sawyer et al., 2008; Winters et al., 2008). We considered the clay-sized fraction to be all grains smaller than  $4 \mu\text{m}$  diameter for consistency with Daigle and Screaton (2015a, 2015b). Gamma ray values exhibit a positive correlation with clay content since the main natural gamma ray-producing isotopes –  $^{40}\text{K}$ ,  $^{232}\text{Th}$ , and  $^{238}\text{U}$  – are generally associated with clay minerals (Ellis and Singer, 2007). Daigle and Dugan (2009) showed that the gamma ray log from KC151-2 correlated positively with specific surface measurements of samples from KC151-3, suggesting that the gamma ray log responded mainly to clay mineral abundance since clay minerals have significantly higher specific surface values than other minerals (Santamarina et al., 2002). In the present analysis, we sought to determine the relationship between gamma ray and clay-sized grain abundance. The clay-sized fraction can include both clay minerals and non-clay minerals, but in shallow sediments in the northern Gulf of Mexico clay minerals tend to be restricted to the clay-sized fraction, in which they are the main component (e.g., John and Adatte, 2009).

The grain size data exhibited a linear dependence on normalized gamma ray (Fig. 11). To construct a relationship, we used endpoint values based on the 1st and 99th percentiles of the normalized gamma ray distributions (Fig. 10b), which were 25 and 100, respectively. We found the relationship  $f_c = 0.0133GR_n - 0.3343$ , where  $GR_n$  is the normalized gamma ray value. This trend fits the data well and honors the normalized gamma ray values.

#### 4.4. Endmember permeabilities

The use of Eq. (2) for permeability prediction requires endmember permeabilities for the clay-sized and (silt + sand)-sized fractions. Daigle and Screaton (2015b) used endmember values based on a global database of permeabilities of sediments from convergent margins. In their study, they used endmember permeability-porosity relationships to define the endmember permeabilities at a given porosity, under the assumption that grain-scale variations in porosity do not deviate significantly from the bulk sediment porosity. Therefore in the present work we assumed that the porosities of the high- and low-permeability endmembers were equal to the porosity of the bulk sediment.

Since the Gulf of Mexico was not included in the data set examined by Daigle and Screaton (2015a), the endmember permeabilities determined by these authors are probably not appropriate. For the high-permeability endmember, we used a database

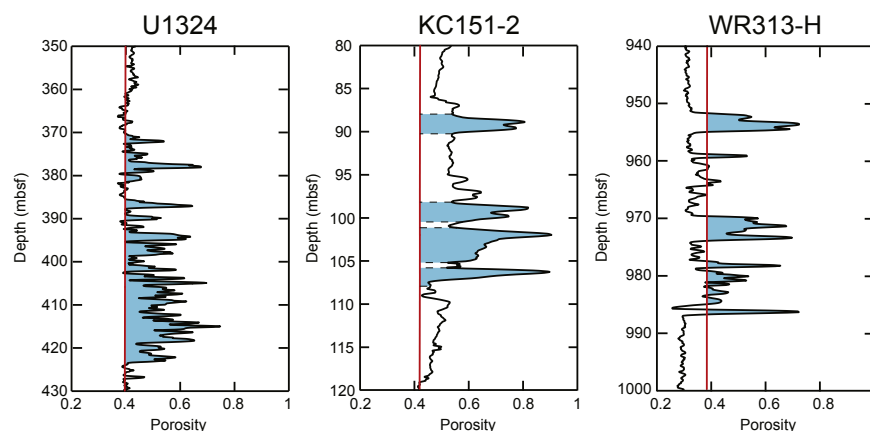


**Fig. 9.** Examples of porosity correction in water-saturated sands with poor borehole conditions. Black lines are original density porosity, red lines are determined from porosity-effective stress relationship. Cyan shaded areas indicate sections where porosity was corrected. Left: deep sands in U1324. Middle: shallow sands at KC151-2. Right: Green sands at WR313-H. (For interpretation of the references to colour in this figure legend, the reader is referred to the web version of this article.)

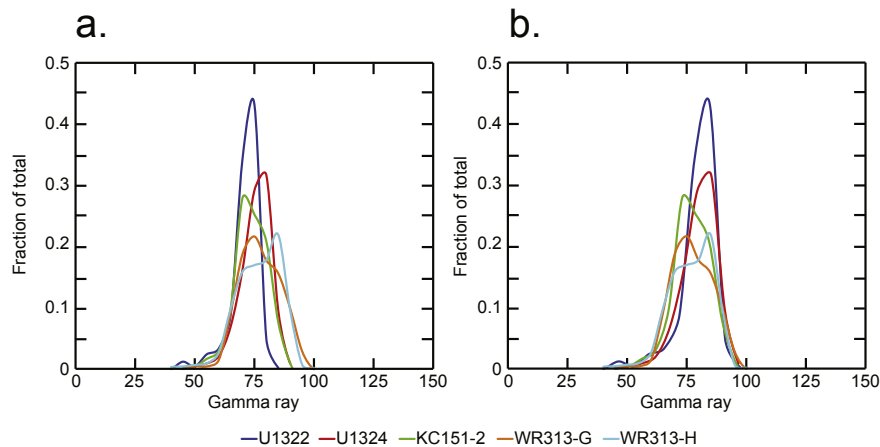


**Fig. 10.** (a) Histogram of raw gamma ray values. (b) Histogram of normalized gamma ray values. Colors represent data from different boreholes. (For interpretation of the references to colour in this figure legend, the reader is referred to the web version of this article.)

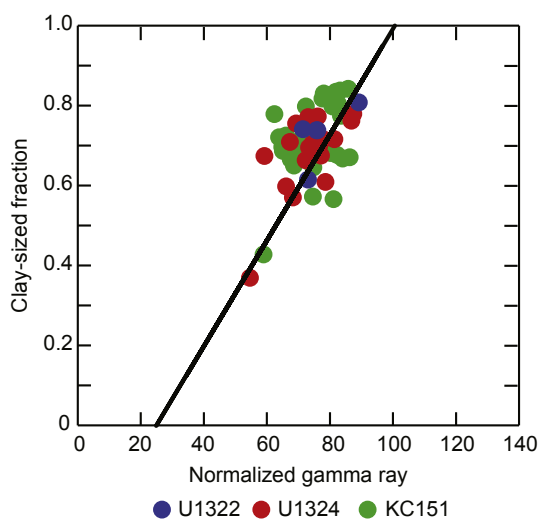


**Fig. 11.** Relationship between normalized gamma ray values ( $GR_n$ ) and clay-sized fraction ( $f_c$ ). Black line is  $f_c = 0.0133GR_n - 0.3343$ .

of porosity and permeability data from the Late Paleocene/Early Eocene Wilcox Group sandstones in the Louisiana and Texas Gulf Coast region (Dutton and Loucks, 2014). The depositional setting of the Wilcox Group ranged from proximal fluvial-deltaic settings to distal turbidites and basin floor fans (Meyer et al., 2007). We therefore believe that the Wilcox, particularly the distal facies, represents a good analog to the turbidite and channel levee sands encountered at the locations we studied. We specifically selected the portion of the database corresponding to low-temperature ( $<100\text{ }^{\circ}\text{C}$ ) settings offshore Louisiana since diagenetic alteration was found to be minimal in this environment, allowing primary depositional fabrics and pore types to be preserved despite the greater age of the Wilcox compared to the sands we considered in the present analysis (Dutton and Loucks, 2014). We found the relationship  $\log_{10}k_s = 2.63 \ln \phi - 9.58$ . For the low-permeability endmember, we used data from uniaxial consolidation tests for mixtures of Na-montmorillonite and silica at clay fractions greater than 0.85 (Daigle, 2011). This resulted in the relationship  $\log_{10}k_c = 6.23\phi - 24.9$ . Variation of  $k_s$  and  $k_c$  with porosity are shown in Fig. 12.

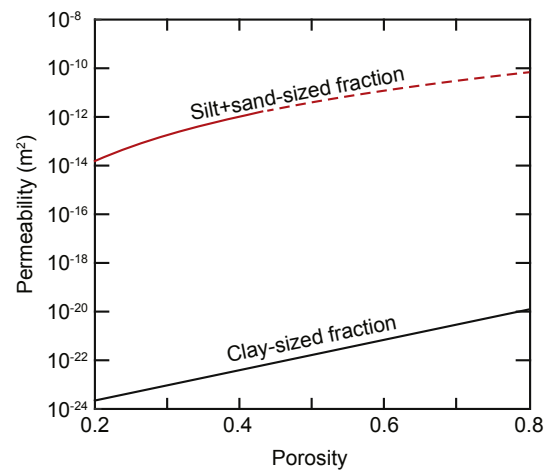


**Fig. 12.** Endmember permeability values versus porosity. Silt + sand-sized fraction line is dashed above porosity of 0.42 since these porosity values are not expected for this endmember based on the porosity-effective stress model we developed based on the data of Zimmer (2003).

## 5. Results and discussion

### 5.1. Model verification

To test whether our procedure accurately predicts known permeability values, we compared predictions to permeability measurements from U1322, U1324, and KC151-3 made by Long et al. (2008b), Dugan (2008), and Daigle and Dugan (2009). All permeability measurements were made using uniaxial, constant rate-of-strain consolidation tests (ASTM International, 2006) using identical equipment (Geotac Sigma-1 from Trautwein Soil Testing Equipment Co.), so we do not expect any systematic variation among the reported values due to differences in technique. We excluded samples collected using the extended core barrel (XCB) system since XCB samples are prone to significant coring-induced disturbance such as biscuiting and remolding that adversely affects permeability measurements (Daigle and Screatton, 2015a). In total we compared predictions against 5 measurements from U1322, 18 measurements from U1324, and 11 measurements from KC151-3. Porosity values were obtained from experimental data,



and the clay-sized fraction was computed from the normalized gamma ray value at the depth corresponding to the sample depth. The predicted permeability values match the measured values well (Fig. 13), with a 95% confidence interval ( $\pm 2\sigma$ ) of 0.62 orders of magnitude and  $R^2 = 0.456$ . Therefore we conclude that our method results in accurate permeability values.

Results for U1322 are shown in Fig. 14. U1322 exhibits a relatively homogeneous lithology, with clay-sized fraction generally between 0.5 and 0.7 except for a clay-rich unit above 28 mbsf that was also noted in shipboard core description (Expedition 308 Scientists, 2006b). Porosity decreases with depth except for a sharp increase around 128 mbsf corresponding to the base of a mass transport deposit. After a decrease in the first 30 mbsf, permeability is between  $10^{-16}$  and  $10^{-17}$  m<sup>2</sup>, decreasing slowly with depth.

Results for U1324 are shown in Fig. 15. The shallow section is similar to that at U1322, with clay-sized fraction between 0.5 and 0.7 down to ~364 mbsf. Below this, sand and silt layers are evident from the variability in clay-sized fraction. This lower unit is interpreted as having been deposited by unconfined turbidity currents in the vicinity of low-relief channels (Expedition 308 Scientists, 2006c). Above 364 mbsf, a single confining channel developed in the area, restricting deposition of sand and silts to the channel itself and resulting in mainly clay being deposited in the vicinity of U1324. The permeability varies between a clay baseline of  $10^{-16}$ – $10^{-17}$  m<sup>2</sup> and closer to  $10^{-16}$  m<sup>2</sup> in the sand and silt layers. This relatively low permeability even in the sands is consistent with lithological description of these layers as silt and very fine sand (Expedition 308 Scientists, 2006c). We note in particular that the low permeability in the very fine sand layers around 400 mbsf is attributable to the presence of a small amount of clay-sized particles ( $f_c \sim 0.03$ ), illustrating the large effect that even a small amount of clay-sized particles has on permeability.

Results for KC151-2 are shown in Fig. 16. Clay-sized fraction is variable between 0.4 and 0.9 with the exception of some sandy layers around 100 and 150 mbsf. The permeability varies between a baseline of roughly  $10^{-17}$  m<sup>2</sup> and a maximum of about  $10^{-12}$  m<sup>2</sup> in the sand layers at 102 mbsf. The coarser-grained layers near the base of the MHSZ (around 350 mbsf) that were interpreted to be hydrate-bearing (Lee and Collett, 2008) have relatively low permeabilities of around  $10^{-16}$  m<sup>2</sup>. This is due to the fact that these

sandier layers are very fine-grained and probably do not represent good reservoir-quality rock. Permeability was not computed at KC151-3 because LWD logs were not collected in this borehole.

### 5.2. Permeability determination at WR313

Results for WR313-G are shown in Fig. 17. Clay-sized fraction is quite variable between a background value of around 0.6–0.7 and values approaching zero in the sands, particularly in the Blue unit. Permeability in the clays decreases from  $10^{-17}$  m<sup>2</sup> to  $10^{-18}$  m<sup>2</sup> with depth. The fractured interval from about 240 to 380 mbsf has a uniformly low permeability, but the top of the interval appears to coincide with a sharp decrease in permeability related to a decrease in porosity. Permeabilities within the best sections of the Blue unit approach  $10^{-12}$  m<sup>2</sup> in the coarsest-grained layers. In the Orange unit, the permeability is quite low because this unit occurs as a mud-filled channel at this location (Boswell et al., 2012b). The base of the MHSZ at WR313-G occurs in a fine-grained interval with very low permeability ( $<10^{-18}$  m<sup>2</sup>).

Results for WR313-H are shown in Fig. 18. The general trends are very similar to those observed in WR313-G. Clay-sized fraction varies with a background value of 0.6–0.7 and values approaching zero in the sands. Permeability in the fine-grained intervals decreases from  $10^{-17}$  m<sup>2</sup> to  $10^{-18}$  m<sup>2</sup> with depth. The fractured interval from about 160 to 305 mbsf is delineated by a sharp decrease in permeability at the top, corresponding to a decrease in porosity. A thin, hydrate-bearing sand near the base of the fractured zone (the “Unit A sand” of Cook and Malinverno (2013)) has a permeability of  $10^{-13}$  m<sup>2</sup>. The sands of the Blue unit have low permeability ( $\sim 10^{-17}$  m<sup>2</sup>), which is consistent with observations by Boswell et al. (2012b) that the Blue unit at WR313-H is a much more distal facies than at WR313-G, with thinner, lower-quality sands. The sands of the Orange unit have permeabilities around  $10^{-13}$  m<sup>2</sup>, reflecting the positioning of WR313-H in proximal levee deposits (Boswell et al., 2012b). The Green unit, below the base of the MHSZ, has similar permeabilities around  $10^{-13}$  m<sup>2</sup>.

### 5.3. Implications for methane migration at Walker Ridge 313

Migration of methane to form hydrate deposits can occur by advection, either as a dissolved phase in water flow or as a discrete gas phase, or by diffusion of dissolved methane. Examples of systems in which only one of these mechanisms is active are rare, but many study locations have been classified as having one mechanism being more important than the other. For example, advection has been proposed to be the main mode of methane transport into the MHSZ at Hydrate Ridge offshore Oregon (Daigle and Dugan, 2010; Daigle, 2011) and at some locations in the Ulleung Basin offshore Korea (Kim et al., 2011, 2012), while diffusion has been shown to be a possible methane transport mechanism in northern Cascadia (Malinverno, 2010), the Nankai Trough (Waseda and Uchida, 2004; Malinverno and Goldberg, 2015), and the Krishna–Godavari Basin offshore India (Malinverno and Goldberg, 2015).

Advective methane transport requires suitable permeable pathways. From Darcy’s law, under a uniform overpressure gradient the ratio of fluid flux through sands to that through adjacent clays is equal to the ratio of their respective permeabilities. For instance, in the Blue unit at WR313-G (Fig. 17), the flux through the sand layers would be 6 orders of magnitude greater than the flux through the adjacent clays under the same overpressure gradient. Numerical simulations have shown that the rate of hydrate accumulation is linearly proportional to the local fluid flux (Chatterjee et al., 2014), so our permeability calculations suggest that hydrate would initially accumulate  $10^5$ – $10^6$  times more rapidly in the sands of the Blue and Orange units at Walker Ridge than in the adjacent clays

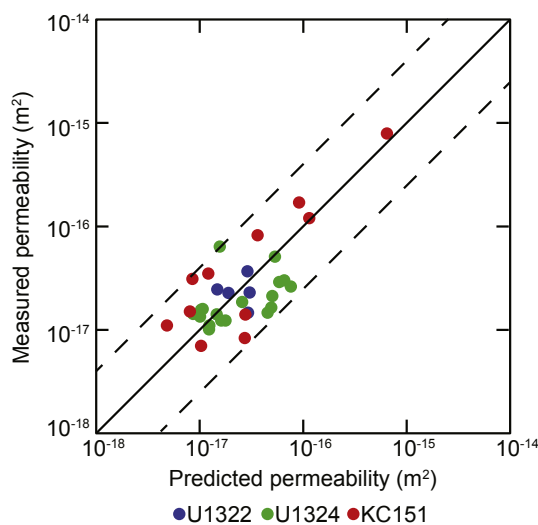


Fig. 13. Model verification showing predicted versus measured permeability values for U1322, U1324, and KC151. Solid line is 1:1 correspondence; dashed lines are two standard deviations ( $\pm 0.62$  orders of magnitude).

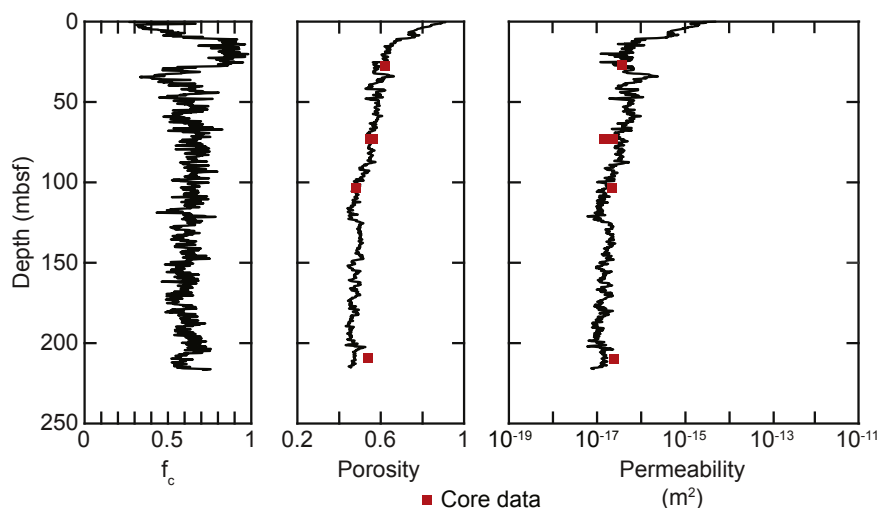


Fig. 14. Calculation results for U1322. Left to right: clay-sized fraction ( $f_c$ ), porosity, permeability. Core porosities and permeabilities are from Long et al. (2008b).

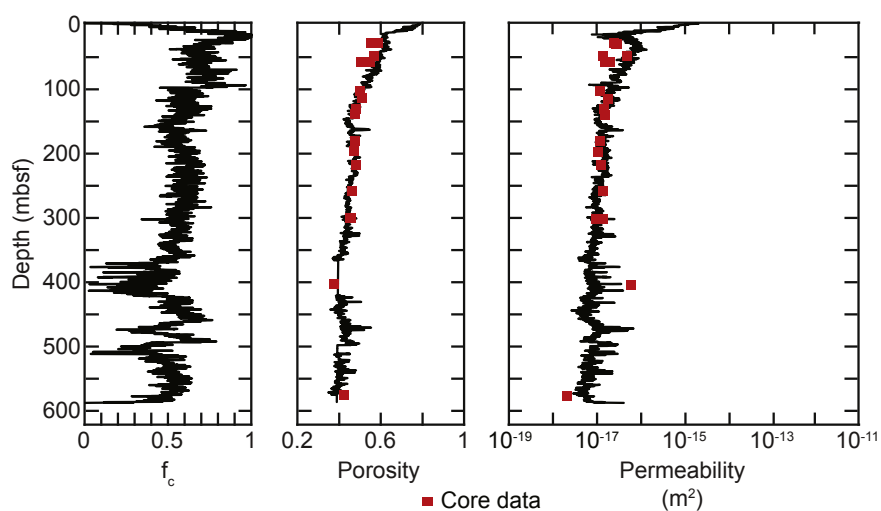


Fig. 15. Calculation results for U1324. Left to right: clay-sized fraction ( $f_c$ ), porosity, permeability. Core porosities and permeabilities are from Long et al. (2008b).

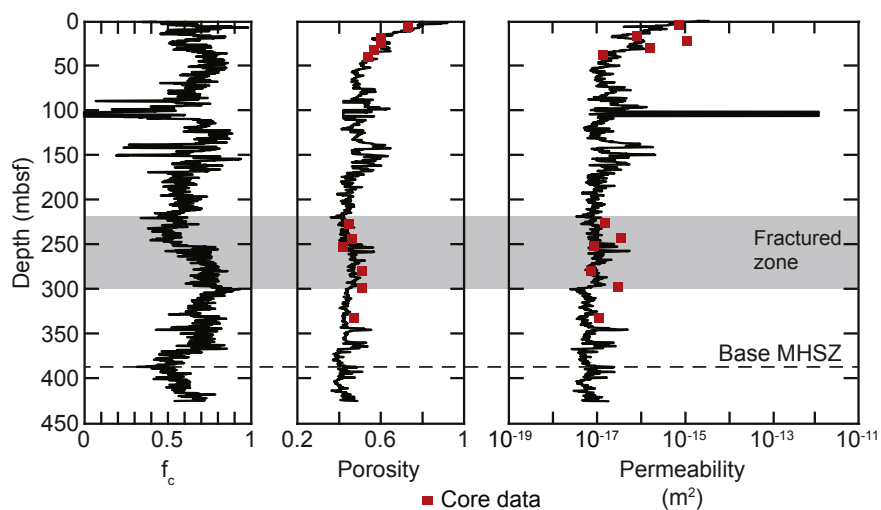


Fig. 16. Calculation results for KC151-2. Left to right: clay-sized fraction ( $f_c$ ), porosity, permeability. Core porosities and permeabilities are from Dugan (2008) and Daigle and Dugan (2009).

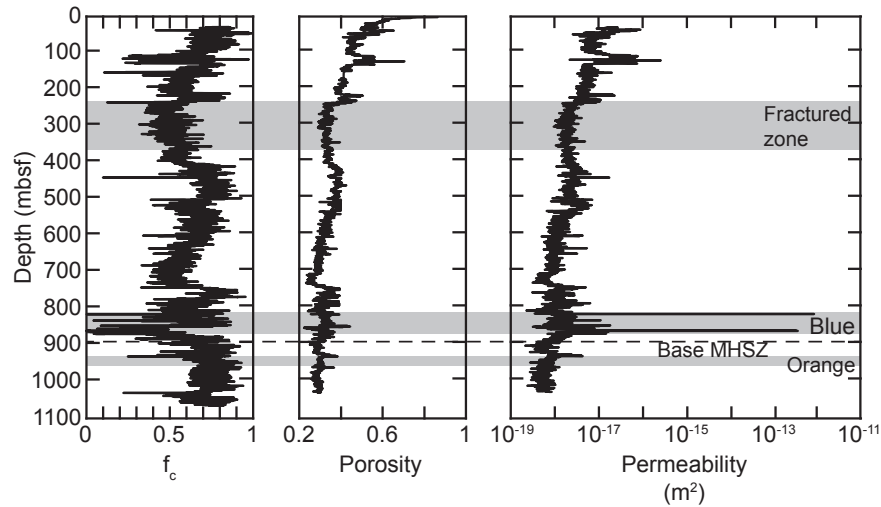


Fig. 17. Calculation results for WR313-G. Left to right: clay-sized fraction ( $f_c$ ), porosity, permeability.

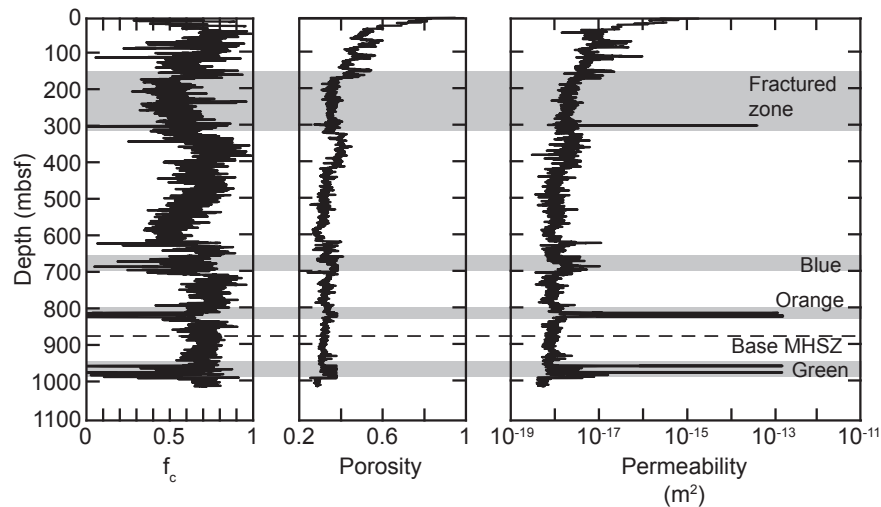


Fig. 18. Calculation results for WR313-H. Left to right: clay-sized fraction ( $f_c$ ), porosity, permeability.

under conditions of advective methane supply. In contrast, the Blue unit in WR313-H (Fig. 18) has only one order of magnitude permeability contrast between the sands and clays, but this is still sufficient to cause preferential flow through the sands. We note that the permeability in the Blue sands in WR313-H is significantly reduced by only a small amount of clay ( $f_c < 0.1$ ), highlighting the large effect that clay-sized grains can have on reservoir quality. It is possible, however, that the clay-sized fraction we determined in the Blue sands at WR313-H were affected by log resolution. The gamma ray log has a vertical resolution of 46 cm (Collett et al., 2012) and would not have yielded the true properties of any sand layers thinner than this. If the Blue sands at WR313-H truly have lower permeability than their stratigraphic equivalents at WR313-G and are connected between the boreholes, the lower updip permeability would limit the flux in the downdip sands. The connectivity of these sands, which may have thicknesses below log resolution, is an extremely important consideration in modeling the system.

As noted at the outset, our permeability estimates are for water-saturated conditions. Advection of methane along sand layers within the MHSZ can quickly become much more difficult as gas hydrate forms occupying the pore space and reducing the absolute

permeability (e.g., Johnson et al., 2011; Kneafsey et al., 2011; Dai and Seol, 2014). For example, in the Orange sand unit in WR313-H, we estimate the permeability is  $10^{-13}$  (Fig. 18) with a corrected water-filled porosity of 0.35–0.45 (Fig. 7). We know, however, that gas hydrate fills the sand layers in the Orange sand, occupying more than 80% of the pore volume in the upper lobe and 60–80% in the lower lobe. In the upper Orange sand lobe, this means that the original porosity of ~0.35 is effectively reduced to ~0.07 due to the presence of gas hydrate, which is bound to considerably reduce the permeability. Recent analyses of the permeability and acoustic velocities of pressure cores of hydrate-bearing sediments from the eastern Nankai Trough (Priest et al., 2014; Konno et al., 2015a; Santamarina et al., 2015) suggest that the hydrate that forms preferentially in sand layers occurs in a pore-filling morphology. The reduced permeability in such a case may be modeled by

$$k = k_0 \frac{(1 - S_h)^3}{(1 + 2S_h)^2}, \quad (8)$$

where  $k_0$  is the permeability of the hydrate-free sediment and  $S_h$  is

the hydrate saturation (Dai and Seol, 2014). In the upper lobe of the Orange sand in WR313-H, with  $k_0 = 10^{-13} \text{ m}^2$  and  $S_h = 80\%$ , Eq. (8) yields a reduced permeability of  $10^{-16} \text{ m}^2$ . Even at such a high hydrate saturation, this reduced permeability is still two orders of magnitude greater than the permeability of the surrounding clay layers;  $S_h = 95\%$  would be required for the sand permeability to be reduced to the same value as the surrounding clays ( $10^{-18} \text{ m}^2$ ). The Blue sands in WR313-G, with  $k_0 = 10^{-12} \text{ m}^2$  and  $S_h = 90\%$  (Collett et al., 2012) have a reduced permeability of  $10^{-16} \text{ m}^2$ , while the Blue sands in WR313-H, with  $k_0 = 10^{-17} \text{ m}^2$  and  $S_h = 80\%$  (Collett et al., 2012), have a reduced permeability of  $10^{-20} \text{ m}^2$ . Thus the Blue sands at WR313-H appear to be the only sands we considered that contain enough hydrate to eliminate preferential flow.

Diffusive methane transport requires a contrast in solubility caused by differences in grain size due to the Gibbs–Thomson effect (Clennell et al., 1999). The Gibbs–Thomson effect is a depression in the three-phase equilibrium temperature caused by the curvature of the hydrate–water interface which results in an increase in methane solubility. The increase in solubility is given by

$$\ln \frac{c_m}{c_{m0}} = \frac{2\gamma}{r} \frac{n\bar{V}_\beta}{RT}, \quad (9)$$

where  $c_{m0}$  is the solubility in the absence of the Gibbs–Thomson effect,  $c_m$  is the solubility in a pore of radius  $r$ ,  $\gamma_{hw}$  is the interfacial energy of the hydrate–water interface ( $0.027 \text{ J m}^{-2}$ ; Waite et al., 2009),  $n$  is the hydrate stoichiometry factor (5.75; Sloan and Koh, 2007),  $\bar{V}_\beta$  is the molar volume of water in the hydrate lattice ( $2.26 \times 10^{-5} \text{ m}^3 \text{ mol}^{-1}$ ; Henry et al., 1999),  $R$  is the universal gas constant ( $8.314 \text{ J mol}^{-1} \text{ K}^{-1}$ ), and  $T$  is absolute temperature [K]. The solubility contrast between sands and clays that arises because of contrasts in pore size drives dissolved methane from clays, where solubility is higher, into sands, where solubility is lower (Malinverno, 2010).

The contrast in pore sizes between the sands and clays at WR313-G and WR313-H may be estimated from the permeability contrast. From the Kozeny–Carman equation,  $k_{sand}/k_{clay} = r_{sand}^2/r_{clay}^2$  where  $k_{sand}$  and  $k_{clay}$  are the sand and clay permeabilities and  $r_{sand}$  and  $r_{clay}$  are the sand and clay pore radii. This relationship assumes that the difference in tortuosities between the sands and clays is less than an order of magnitude (Boudreau and Meysman, 2006) and that the pore shape factor is not significantly different between the sand and clays (the pore shape factor only varies between 1.2 and 3 for a wide range of pore shapes; Carman, 1937). The sand near the base of the fractured zone in WR313-H (Fig. 18) has a permeability contrast of roughly  $10^5$  with the surrounding clay. Cook and Malinverno (2013) modeled diffusive migration of microbial methane into this sand and found that the methane flux is sufficient to form hydrate within a few hundred thousand years. They based their model on a clay pore size of 100 nm and a pore size in the sand that is large enough not to cause a significant change in solubility relative to bulk seawater. Assuming a clay pore size of 100 nm, which is reasonable for marine clays (e.g., Henry et al., 1999; Liu and Flemings, 2011; Day–Stirrat et al., 2012; Daigle and Dugan, 2014), the permeability contrast implies that  $r_{sand} = 30 \text{ }\mu\text{m}$ . Using this value for  $r$  in Eq. (9) along with  $T = 282.2 \text{ K}$  (Cook and Malinverno, 2013) yields  $c_m/c_{m0} = 1.00$ , so the assumption that solubility in the sand is equal to the bulk value is valid. Similar pore size contrasts, and thus solubility gradients, may be expected in the Blue unit in WR313-G (Fig. 17) and the Orange unit in WR313-H (Fig. 18), based on the permeability contrast of order  $10^5$  between the sands and clays. The Blue unit in WR313-H (Fig. 18), on the other hand, has a permeability contrast of only 10 between the sands and clays. Assuming that clay is evenly dispersed throughout the sands, this implies a pore size of 300 nm in the sands due to the higher

abundance of clay-sized grains. The solubility in these sands is 1.01 times the value in bulk seawater, compared with a contrast of 1.03 in the clays. This means that the methane concentration gradient is roughly 75% of the value present in the shallow sand modeled by Cook and Malinverno (2013), and the methane flux driven by diffusion would be 75% of the value in the shallow sand. The pore size in the Blue unit sands in WR313-H could be larger, however, if our calculated clay-sized fractions are overestimated due to gamma ray tool resolution. Overall the permeability and pore size contrasts between the clays and sands will have a greater influence on advective methane transport than on diffusion of dissolved methane since the corresponding reductions in methane flux would be several orders of magnitude in the case of advection compared with less than one order of magnitude in the case of diffusion.

## 6. Conclusions

Using effective medium theory we determined permeability in five boreholes in the northern Gulf of Mexico by considering the sediments as a mixture of clay-sized and larger particles. Our method consisted of determining clay-sized fraction from normalized gamma ray logs and computing permeability using endpoint permeability values defined by laboratory measurements of Wilcox Group sandstones and silica-montmorillonite mixtures. We showed that the method yielded permeability values that matched measured values in three boreholes, and used the method to predict permeability in two boreholes at Walker Ridge for which no permeability measurements were available.

In the two boreholes at Walker Ridge, we found that hydrate-bearing sands encountered during drilling had 5–6 orders of magnitude permeability contrast with the surrounding clays. This level of permeability contrast would be sufficient to partition hydrate formation into the sands alone if methane were supplied by fluid advection from some deep source. However, in one particular sand (the Blue unit in WR313-H), only one order of magnitude permeability contrast was predicted, which would not be sufficient for significant focusing of hydrate formation due to focused flow. On the other hand, our permeability estimates in this instance may be limited by the vertical resolution of the LWD logs, causing us to overestimate the clay-sized fraction and underestimate permeability. Considering the hydrate saturations estimated from logs in these sands, in most cases the corresponding reductions in permeability due to the presence of the hydrate would still allow focused flow with 2 orders of magnitude permeability contrast with the surrounding clays. Estimates of pore size differences and resulting solubility contrasts suggested that diffusive flux of methane from the clays into the sands would remain significant even where the permeability contrast was only one order of magnitude, possibly allowing methane generated in the clays to form hydrate in the sand layers. Our results show that advection or diffusion can be effective means of forming hydrate in the cleanest, high-permeability sands ( $f_c < 0.05$ ), but that the relative importance of diffusion as a means of methane transport increases in sands with larger clay-sized fractions and lower permeabilities.

## Acknowledgments

The authors thank R. Boswell and W. Waite for helpful reviews that strengthened this manuscript.

This material is based upon work supported by the Department of Energy under Award Number DE-FE0013919. This report was prepared as an account of work sponsored by an agency of the United States Government. Neither the United States Government nor any agency thereof, nor any of their employees, makes any



warranty, express or implied, or assumes any legal liability or responsibility for the accuracy, completeness, or usefulness of any information, apparatus, product, or process disclosed, or represents that its use would not infringe on privately owned rights. Reference herein to any specific commercial product, process, or service by trade name, trademark, manufacturer, or otherwise does not necessarily constitute or imply its endorsement, recommendation, or favoring by the United States Government or any agency thereof. The views and opinions of authors expressed herein to not necessarily state or reflect those of the United States Government or any agency thereof.

## References

- ASTM International, 2003. Standard Test Method for Particle-size Analysis of Soils, pp. D422–D463.
- ASTM International, 2006. Standard Test Method for One-dimensional Consolidation Properties of Saturated Cohesive Soils Using Controlled-strain Loading, 41866–D4206.
- Behrmann, J.H., Flemings, P.B., John, C.M., IODP Expedition 308 Scientists, 2006. Rapid sedimentation, overpressure, and focused fluid flow, Gulf of Mexico continental margin. *Sci. Drill.* 3, 12–17. <http://dx.doi.org/10.2204/iodp.sd.3.03.2006>.
- Boswell, R., Collett, T.S., Frye, M., Shedd, W., McConnell, D.R., Shelander, D., 2012a. Subsurface gas hydrates in the northern Gulf of Mexico. *Mar. Pet. Geol.* 34 (1), 4–30. <http://dx.doi.org/10.1016/j.marpetgeo.2011.10.003>.
- Boswell, R., Frye, M., Shelander, D., Shedd, W., McConnell, D.R., Cook, A., 2012b. Architecture of gas-hydrate-bearing sands from Walker Ridge 313, Green Canyon 955, and Alaminos Canyon 21: northern deepwater Gulf of Mexico. *Mar. Pet. Geol.* 34 (1), 134–149. <http://dx.doi.org/10.1016/j.marpetgeo.2011.08.010>.
- Boudreau, B.P., Meysman, F.J.R., 2006. Predicted tortuosity of muds. *Geology* 34 (8), 693–696. <http://dx.doi.org/10.1130/G22771.1>.
- Carman, P.C., 1937. Fluid Flow through Granular Beds, vol. 15. Transactions of the Institution of Chemical Engineers of London, pp. 150–166.
- Chatterjee, S., Bhatnagar, G., Dugan, B., Dickens, G.R., Chapman, W.G., Hirasaki, G.J., 2014. The impact of lithologic heterogeneity and focused fluid flow upon gas hydrate distribution in marine sediments. *J. Geophys. Res. B Solid Earth* 119 (9), 6705–6732. <http://dx.doi.org/10.1002/2014JB011236>.
- Claypool, G. (Ed.), 2006. Cruise Report: the Gulf of Mexico Gas Hydrate Joint Industry Project. Shipboard Scientific Party. <https://www.netl.doe.gov/File%20Library/Research/oil-gas/methane%20hydrates/GOM/JIP/Cruise05.pdf>.
- Clennell, M.B., Hovland, M., Booth, J.S., Henry, P., Winters, W.J., 1999. Formation of natural gas hydrates in marine sediments 1. Conceptual model of gas hydrate growth conditioned by host sediment properties. *J. Geophys. Res.* 104 (B10), 22985–23003. <http://dx.doi.org/10.1029/1999JB900175>.
- Collett, T.S., Lee, M.W., Zyrianova, M.V., Mrozeński, S.A., Guerin, G., Cook, A.E., Goldberg, D.S., 2012. Gulf of Mexico gas hydrate joint industry project leg II logging-while-drilling data acquisition and analysis. *Mar. Pet. Geol.* 34 (1), 41–61. <http://dx.doi.org/10.1016/j.marpetgeo.2011.08.003>.
- Cook, A.E., Anderson, B.I., Rasmus, J., Sun, K., Li, Q., Collett, T.S., Goldberg, D.S., 2012. Electrical anisotropy of gas hydrate-bearing sand reservoirs in the Gulf of Mexico. *Mar. Pet. Geol.* 34 (1), 72–84. <http://dx.doi.org/10.1016/j.marpetgeo.2011.09.003>.
- Cook, A.E., Goldberg, D., Kleinberg, R.L., 2008. Fracture-controlled gas hydrate systems in the northern Gulf of Mexico. *Mar. Pet. Geol.* 25 (9), 932–941. <http://dx.doi.org/10.1016/j.marpetgeo.2008.01.013>.
- Cook, A.E., Malinverno, A., 2013. Short migration of methane into a gas hydrate-bearing sand layer at Walker Ridge, Gulf of Mexico. *Geochim. Geophys. Geosyst.* 14 (2), 283–291. <http://dx.doi.org/10.1002/ggge.20040>.
- Dai, S., Seol, Y., 2014. Water permeability in hydrate-bearing sediments: a pore-scale study. *Geophys. Res. Lett.* 41 (12), 4176–4184. <http://dx.doi.org/10.1002/2014GL060535>.
- Daigle, H., 2011. Pore-scale Controls on Permeability, Fluid Flow, and Methane Hydrate Distribution in Fine-grained Sediments (PhD thesis). Rice University, Houston, Texas, USA.
- Daigle, H., Dugan, B., 2009. Extending NMR data for permeability estimation in fine-grained sediments. *Mar. Pet. Geol.* 26 (8), 1419–1427. <http://dx.doi.org/10.1016/j.marpetgeo.2009.02.008>.
- Daigle, H., Dugan, B., 2010. Effects of multiphase methane supply on hydrate accumulation and fracture generation. *Geophys. Res. Lett.* 37 (20), L20301. <http://dx.doi.org/10.1029/2010GL044970>.
- Daigle, H., Dugan, B., 2014. Data report: permeability, consolidation, stress state, and pore system characteristics of sediments from sites C0011, C0012, and C0018 of the Nankai Trough. In: Henry, P., Kanamatsu, T., Moe, K.T., the Expedition 333 Scientists (Eds.), Proceedings of the Integrated Ocean Drilling Program 333. Integrated Ocean Drilling Program Management International, Tokyo, pp. 1–23. <http://dx.doi.org/10.2204/iodp.proc.333.201.2014>.
- Daigle, H., Scream, E.J., 2015a. Evolution of sediment permeability during burial and subduction. *Geofluids* 15 (1–2), 84–105. <http://dx.doi.org/10.1111/gfl.12090>.
- Daigle, H., Scream, E.J., 2015b. An effective medium model for permeability of marine sediments entering subduction zones. *Geophys. Res. Lett.* 42 <http://dx.doi.org/10.1002/2015GL064542>.
- David, C., Gueguen, Y., Pampoukis, G., 1990. Effective medium theory and network theory applied to the transport properties of rock. *J. Geophys. Res.* 95 (B5), 6993–7005. <http://dx.doi.org/10.1029/JB095B05p06993>.
- Day-Stirrat, R.J., Flemings, P.B., You, Y., Aplin, A.C., van der Pluijm, B.A., 2012. The fabric of consolidation in Gulf of Mexico mudstones. *Mar. Geol.* 295–298, 77–85. <http://dx.doi.org/10.1016/j.marpetgeo.2011.12.003>.
- Dugan, B., 2008. Fluid flow in the Keathley Canyon 151 Mini-Basin, northern Gulf of Mexico. *Mar. Pet. Geol.* 25 (9), 919–923. <http://dx.doi.org/10.1016/j.marpetgeo.2007.12.005>.
- Dullien, F.A.L., 1992. Porous Media Fluid Transport and Pore Structure, second ed. Academic Press, San Diego, p. 574.
- Dutton, S.P., Loucks, R.G., 2014. Reservoir quality and porosity-permeability trends in on shore Wilcox sandstones, Texas and Louisiana Gulf Coast: application to deep Wilcox plays, offshore Gulf of Mexico. *GCAGS J.* 3, 33–40.
- Edwards, R.N., 1997. On the resource evaluation of marine gas hydrate deposits using sea-floor transient electric dipole methods. *Geophysics* 62 (1), 63–74. <http://dx.doi.org/10.1190/1.1444146>.
- Ellis, D.V., Singer, J.M., 2007. Well Logging for Earth Scientists, second ed. Springer, Dordrecht, p. 708.
- Expedition 308 Scientists, 2006a. Methods. In: Flemings, P.B., Behrmann, J.H., John, C.M., the Expedition 308 Scientists (Eds.), Proceedings of the Integrated Ocean Drilling Program 308. Integrated Ocean Drilling Program Management International, College Station, TX, pp. 1–44. <http://dx.doi.org/10.2204/iodp.proc.308.102.2006>.
- Expedition 308 Scientists, 2006b. Site U1322. In: Flemings, P.B., Behrmann, J.H., John, C.M., the Expedition 308 Scientists (Eds.), Proceedings of the Integrated Ocean Drilling Program 308. Integrated Ocean Drilling Program Management International, College Station, TX, pp. 1–104. <http://dx.doi.org/10.2204/iodp.proc.308.106.2006>.
- Expedition 308 Scientists, 2006c. Site U1324. In: Flemings, P.B., Behrmann, J.H., John, C.M., the Expedition 308 Scientists (Eds.), Proceedings of the Integrated Ocean Drilling Program 308. Integrated Ocean Drilling Program Management International, College Station, TX, pp. 1–128. <http://dx.doi.org/10.2204/iodp.proc.308.108.2006>.
- Fofonoff, N.P., Millard, R.C., 1983. Algorithms for computation of fundamental properties of seawater. UNESCO Tech. Pap. Mar. Sci. 44.
- Frye, M., 2008. Preliminary Evaluation of In-place Gas Hydrate Resources: Gulf of Mexico Outer Continental Shelf: Minerals Management Service Report 2008-004. <http://www.mms.gov/revaldiv/GasHydrateAssessment.htm>.
- Gaddipati, M., Myshakin, E.M., Boswell, R., Anderson, B.J., 2011. Gas production modeling from a complex 3-D description of marine hydrate deposits. In: 7th International Conference on Gas Hydrates, Edinburgh, Scotland, July 17–21, Paper 691.
- Helgerud, M.B., Waite, W.F., Kirby, S.H., Nur, A., 2009. Elastic wave speeds and moduli in polycrystalline ice Ih, sl methane hydrate, and sl methane-ethane hydrate. *J. Geophys. Res.* 114 (B2), B02212. <http://dx.doi.org/10.1029/2008JB006132>.
- Henry, P., Thomas, M., Clennell, M.B., 1999. Formation of natural gas hydrates in marine sediments 2. Thermodynamic calculations of stability conditions in porous sediments. *J. Geophys. Res.* 104 (B10), 23005–23022. <http://dx.doi.org/10.1029/1999JB900167>.
- Hutchinson, D.R., Hart, P.E., Collett, T.S., Edwards, K.M., Twichell, D.C., Snyder, F., 2008. Geologic framework of the 2005 Keathley Canyon gas hydrate research well, northern Gulf of Mexico. *Mar. Pet. Geol.* 25 (9), 906–918. <http://dx.doi.org/10.1016/j.marpetgeo.2008.01.012>.
- John, C.M., Adatte, T., 2009. Data report: X-ray analyses of bulk sediment in IODP Holes U1320A and U1324B, northern Gulf of Mexico. In: Flemings, P.B., Behrmann, J.H., John, C.M., the Expedition 308 Scientists (Eds.), Proceedings of the Integrated Ocean Drilling Program 308. Integrated Ocean Drilling Program Management International, College Station, TX, pp. 1–19. <http://dx.doi.org/10.2204/iodp.proc.308.214.2009>.
- Johnson, A., Patil, S., Dandekar, A., 2011. Experimental investigation of gas-water relative permeability for gas-hydrate-bearing sediments from the Mount Elbert gas hydrate stratigraphic test well, Alaska North Slope. *Mar. Pet. Geol.* 28 (2), 419–426. <http://dx.doi.org/10.1016/j.marpetgeo.2009.10.013>.
- Kim, J.-H., Park, M.-H., Chun, J.-H., Lee, J.Y., 2011. Molecular and isotopic signatures in sediments and gas hydrate of the central/southwestern Ulleung Basin: high alkalinity escape fuelled by biogenically sourced methane. *Geo-Mar. Lett.* 31, 37–48. <http://dx.doi.org/10.1007/s00367-010-0214-y>.
- Kim, J.-H., Torres, M.E., Choi, J., Bahk, J.-J., Park, M.-H., Hong, W.-L., 2012. Inferences on gas transport based on molecular and isotopic signatures of gases at acoustic chimneys and background sites in the Ulleung Basin. *Org. Geochem.* 43, 26–38. <http://dx.doi.org/10.1016/j.orggeochem.2011.11.004>.
- Kirkpatrick, S., 1971. Classical transport in disordered media: scaling and effective-medium theories. *Phys. Rev. Lett.* 27 (25), 1722–1725. <http://dx.doi.org/10.1103/physrevlett.27.1722>.
- Kirkpatrick, S., 1973. Percolation and conduction. *Rev. Mod. Phys.* 45 (4), 574–588. <http://dx.doi.org/10.1103/revmodphys.45.574>.
- Kneafsey, T.J., Seol, Y., Gupta, A., Tomutsa, L., 2011. Permeability of laboratory-formed methane-hydrate bearing sand: measurements and observations using X-ray computed tomography. *SPE J.* 16 (1), 78–94. <http://dx.doi.org/10.2118/139525-PA>.



- Konno, Y., Jin, Y., Yoneda, J., Kida, M., Egawa, K., Ito, T., Suzuki, K., Nagao, J., 2015a. Effect of methane hydrate morphology on compressional wave velocity of sandy sediments: analysis of pressure cores obtained in the Eastern Nankai Trough. *Mar. Pet. Geol.* 66, 425–433. <http://dx.doi.org/10.1016/j.marpetgeo.2015.02.021>.
- Konno, Y., Yoneda, J., Egawa, K., Ito, T., Jin, Y., Kida, M., Suzuki, K., Fujii, T., Nagao, J., 2015b. Permeability of sediment cores from methane hydrate deposit in the Eastern Nankai Trough. *Mar. Pet. Geol.* 66, 487–495. <http://dx.doi.org/10.1016/j.marpetgeo.2015.02.020>.
- Lee, M.W., Collett, T.S., 2008. Integrated analysis of well logs and seismic data to estimate gas hydrate concentrations at Keathley Canyon, Gulf of Mexico. *Mar. Pet. Geol.* 25 (9), 924–931. <http://dx.doi.org/10.1016/j.marpetgeo.2007.09.002>.
- Long, H., Flemings, P.B., Dugan, B., Germaine, J.T., Ferrell, D., 2008a. Data report: penetrometer measurements of in situ temperature and pressure, IODP Expedition 308. In: Flemings, P.B., Behrmann, J.H., John, C.M., the Expedition 308 Scientists (Eds.), Proceedings of the Integrated Ocean Drilling Program 308. Integrated Ocean Drilling Program Management International, College Station, TX, pp. 1–68. <http://dx.doi.org/10.2204/iodp.proc.308.203.2008>.
- Long, H., Flemings, P.B., Germaine, J.T., Saffer, D.M., Dugan, B., 2008b. Data report: consolidation characteristics of sediments from IODP Expedition 308, Ursa Basin, Gulf of Mexico. In: Flemings, P.B., Behrmann, J.H., John, C.M., the Expedition 308 Scientists (Eds.), Proceedings of the Integrated Ocean Drilling Program 308. Integrated Ocean Drilling Program Management International, College Station, TX, pp. 1–47. <http://dx.doi.org/10.2204/iodp.proc.308.204.2008>.
- Liu, X., Flemings, P.B., 2011. Capillary effects on hydrate stability in marine sediments. *J. Geophys. Res.* 116, B07102. <http://dx.doi.org/10.1029/2010JB008143>.
- Liu, X., Flemings, P.B., 2009. Dynamic response of oceanic hydrates to sea level drop. *Geophys. Res. Lett.* 36 (17), L17308. <http://dx.doi.org/10.1029/2009GL039821>.
- Malinverno, A., 2010. Marine gas hydrates in thin sand layers that soak up microbial methane. *Earth Planet. Sci. Lett.* 292, 399–408. <http://dx.doi.org/10.1016/j.epsl.2010.1002.1008>.
- Malinverno, A., Goldberg, D.S., 2015. Testing short-range migration of microbial methane as a hydrate formation mechanism: results from Andaman Sea and Kumano Basin drill sites and global implications. *Earth Planet. Sci. Lett.* 422, 105–114. <http://dx.doi.org/10.1016/j.epsl.2015.04.019>.
- McLachlan, D.S., 1988. Measurement and analysis of a model dual-conductivity medium using a generalised effective-medium theory. *J. Phys. C Solid State Phys.* 21 (8), 1521–1532. <http://dx.doi.org/10.1088/0022-3719/21/8/025>.
- Meyer, D., Zarra, L., Yun, J., 2007. From BAHA to Jack, evolution of the lower Tertiary Wilcox trend in the deepwater Gulf of Mexico. *Sediment. Rec.* 5 (3), 4–9.
- Moridis, G.J., Collett, T.S., Dallimore, S.R., Satoh, T., Hancock, S., Weatherill, B., 2004. Numerical studies of gas production from several CH<sub>4</sub> hydrate zones at the Mallik site, Mackenzie Delta, Canada. *J. Pet. Sci. Eng.* 43 (3–4), 219–238. <http://dx.doi.org/10.1016/j.petrol.2004.02.015>.
- Moridis, J.G., Reagan, M.T., Boswell, R., Collett, T., Zhang, K., 2010. Preliminary evaluation of the production potential of recently discovered hydrate deposits in the Gulf of Mexico. In: Offshore Technology Conference, Houston, Texas, May 3–6, Paper OTC-21049. <http://dx.doi.org/10.4043/21049-MS>.
- Myshakin, E.M., Gaddipati, M., Rose, K., Anderson, B.J., 2012. Numerical simulations of depressurization-induced gas production from gas hydrate reservoirs at the Walker Ridge 313 site, northern Gulf of Mexico. *Mar. Pet. Geol.* 34 (1), 169–185. <http://dx.doi.org/10.1016/j.marpetgeo.2011.09.001>.
- Nimblett, J., Ruppel, C., 2003. Permeability evolution during the formation of gas hydrates in marine sediments. *J. Geophys. Res.* 108 (B9), 2420. <http://dx.doi.org/10.1029/2001JB001650>.
- Orange, D.L., Saffer, D., Jeanjean, P., Al-Khafaji, Z., Humphrey, G., Riley, G., 2003. Measurements and modeling of the shallow pore pressure regime at the Sigsbee Escarpment: successful prediction of overpressure and ground-truthing with borehole measurements. *Lead. Edge* 22 (9), 906–913. <http://dx.doi.org/10.1190/1.1614157>.
- Ostermeier, R.M., Pelletier, J.H., Winker, C.D., Nicholson, J.W., Rambow, F.H., Cowan, K.M., 2002. Dealing with shallow-water flow in the deepwater Gulf of Mexico. *Lead. Edge* 21 (7), 660–668. <http://dx.doi.org/10.1190/1.1497320>.
- Priest, J.A., Druce, M., Roberts, J., Schultheiss, P., Nakatsuka, Y., Suzuki, K., 2014. PCATS Triaxial: a new geotechnical apparatus for characterizing pressure cores from the Nankai Trough, Japan. *Mar. Pet. Geol.* 66, 460–470. <http://dx.doi.org/10.1016/j.marpetgeo.2014.12.005>.
- Reagan, M.T., Moridis, G.J., 2008. Dynamic response of oceanic hydrate deposits to ocean temperature change. *J. Geophys. Res.* 113 (C12), C12023. <http://dx.doi.org/10.1029/2008JC004938>.
- Reece, J.S., Flemings, P.B., Germaine, J.T., 2013. Data report: permeability, compressibility, and microstructure of resedimented mudstone from IODP Expedition 322, Site C0011. In: Saito, S., Underwood, M.B., Kubo, Y., the Expedition 322 Scientists (Eds.), Proceedings of the Integrated Ocean Drilling Program 322. Integrated Ocean Drilling Program Management International, Tokyo, Japan, pp. 1–26. <http://dx.doi.org/10.2204/iodp.proc.322.205.2013>.
- Renard, P., de Marsily, G., 1997. Calculating equivalent permeability: a review. *Adv. Water Resour.* 20 (5–6), 253–278. [http://dx.doi.org/10.1016/S0309-1708\(96\)00050-4](http://dx.doi.org/10.1016/S0309-1708(96)00050-4).
- Ruppel, C., Boswell, R., Jones, E., 2008. Scientific results from gulf of Mexico gas hydrates joint industry project leg 1 drilling: Introduction and overview. *Mar. Pet. Geol.* 25 (9), 819–829. <http://dx.doi.org/10.1016/j.marpetgeo.2008.02.007>.
- Santamarina, J.C., Dai, S., Terzariol, M., Jang, J., Waite, W.F., Winters, W.J., Nagao, J., Yoneda, J., Konno, Y., Fujii, T., Suzuki, K., 2015. Hydro-bio-geomechanical properties of hydrate-bearing sediments from Nankai Trough. *Mar. Pet. Geol.* 66, 434–450. <http://dx.doi.org/10.1016/j.marpetgeo.2015.02.033>.
- Santamarina, J.C., Klein, K.A., Wang, Y.H., Prencke, E., 2002. Specific surface: determination and relevance. *Can. Geotech. J.* 39, 233–241. <http://dx.doi.org/10.1139/T01-077>.
- Sawyer, D.E., Jacoby, R., Flemings, P., Germaine, J.T., 2008. Data report: particle size analysis of sediments in the Ursa Basin, IODP Expedition 308 Sites U1324 and U1322, northern Gulf of Mexico. In: Flemings, P.B., Behrmann, J.H., John, C.M., the Expedition 308 Scientists (Eds.), Proceedings of the Integrated Ocean Drilling Program 308. Integrated Ocean Drilling Program Management International, College Station, TX, pp. 1–20. <http://dx.doi.org/10.2204/iodp.proc.308.205.2008>.
- Schneider, J., Flemings, P.B., Day-Stirrat, R.J., Germaine, J.T., 2011. Insights into pore-scale controls on mudstone permeability through resedimentation experiments. *Geology* 39 (11), 1011–1014. <http://dx.doi.org/10.1130/G32475.1>.
- Sloan, E.D., Koh, C., 2007. *Clathrate Hydrates of Natural Gases*, third ed. CRC Press, Boca Raton, p. 752.
- Stow, D.A.V., Cremer, M., Droz, L., Meyer, A.W., Normark, W.R., O'Connell, S., Pickering, K.T., Stelling, C.E., Angell, S.A., Chaplin, C., 1986. Facies, composition, and texture of Mississippi fan sediments, deep sea drilling project leg 96, gulf of Mexico. In: Bauma, A.H., Coleman, J.M., Meyer, A.W., et al. (Eds.), Initial Reports of the Deep Sea Drilling Program 96. United States Government Printing Office, Washington, DC, pp. 475–487. <http://dx.doi.org/10.2973/dsdp.proc.96.121.1986>.
- Waite, W.F., Santamarina, J.C., Cortes, D.D., Dugan, B., Espinoza, D.N., Germaine, J., Jang, J., Jung, J.W., Kneafsey, T.J., Shin, H., Soga, K., Winters, W.J., Yun, T.-S., 2009. Physical properties of hydrate-bearing sediments. *Rev. Geophys.* 47, RG4003. <http://dx.doi.org/10.1029/2008RG000279>.
- Waseda, A., Uchida, T., 2004. The geochemical context of gas hydrate in the eastern Nankai Trough. *Resour. Geol.* 54 (1), 69–78. <http://dx.doi.org/10.1111/j.1751-3928.2004.tb00188.x>.
- Winters, W.J., Dugan, B., Collett, T.S., 2008. Physical properties of sediments from Keathley Canyon and Atwater Valley, JIP Gulf of Mexico gas hydrate drilling program. *Mar. Pet. Geol.* 25 (9), 896–905. <http://dx.doi.org/10.1016/j.marpetgeo.2008.01.018>.
- Xu, W., Germanovich, L.N., 2006. Excess pore pressure resulting from methane hydrate dissociation in marine sediments: a theoretical approach. *J. Geophys. Res.* 111 (B1), B01104. <http://dx.doi.org/10.1029/2004JB003600>.
- Xu, W., Ruppel, C., 1999. Predicting the occurrence, distribution, and evolution of methane gas hydrate in porous marine sediments. *J. Geophys. Res.* 104 (B3), 5081–5095. <http://dx.doi.org/10.1029/1998JB900092>.
- Zimmer, M.A., 2003. *Seismic Velocities in Unconsolidated Sands: Measurements of Pressure, Sorting, and Compaction Effects* (PhD thesis). Stanford University, Stanford, California, USA.